*Materials Research.* 2019; 22(6): e20190417
DOI: http://dx.doi.org/10.1590/1980-5373-MR-2019-0417

# Flexible, Large-Area Organic Solar Cells With Improved Performance Through Incorporation of $CoFe_2O_4$ Nanoparticles in the Active Layer

*Maurício de Sousa Pereira*[a,b,*], *Francisco Anderson de Sousa Lima*[c], *Rodrigo Queiros de Almeida*[d], *Juliana Luiza da Silva Martins*[e], *Diego Bagnis*[e], *Eduardo Bedê Barros*[d], *Antonio Sergio Bezerra Sombra*[b], *Igor Frota de Vasconcelos*[a]

[a]*Departamento de Engenharia Metalúrgica e de Materiais, Universidade Federal do Ceará, Fortaleza, CE, Brasil*
[b]*Laboratório de Telecomunicações e Ciência e Engenharia de Materiais, Universidade Federal do Ceará, Fortaleza, CE, Brasil*
[c]*A2 Group Tecnologia e Serviços, Fortaleza, CE, Brasil*
[d]*Departamento de Física, Universidade Federal do Ceará, Fortaleza, CE, Brasil*
[e]*Divisão Eletrônica Orgânica, Centro Suiço de Eletrônica e Microtecnologia (CSEM), Belo Horizonte, MG, Brasil*

Received: July 05, 2019; Revised: October 24, 2019; Accepted: November 2, 2019

Cobalt ferrite ($CoFe_2O_4$) nanoparticles (NPs), with an average diameter of about 4-10 *nm*, were produced by the proteic sol-gel method and successfully doped into the active layer of poly(3-hexylthiophene-2,5-diyl) (P3HT):[6,6]-phenyl-C61-butyric acid methyl ester (PCBM) organic solar cells. Pristine and $CoFe_2O_4$ NPs-doped blends of P3HT:PCBM were dispersed in a mixture of o-xylene:tetralin (1 mg/mL) based non-halogenated solvents and deposited via a semi-industrial blade coating process on flexible substrates to fabricate large area (0.55 $cm^2$), flexible organic solar cells with inverted configuration. The main focus of this study aims to assess the influence of NPs on the efficiency, stability and lifetime of the produced devices. From the photovoltaic parameters it was observed that the optimization of the bulk-heterojunction through the incorporation of $CoFe_2O_4$ NPs resulted in increased short-circuit current density. As a result, the power conversion efficiency of doped devices increased by 10 % when compared with the undoped reference devices. Tests of lifetime and stability were performed using International Summit on OPV Stability (ISOS) protocols ISOS-D-3, ISOS-O-1 and ISOS-L-1. For the duration of the tests (1200 h), the results showed that doped cells presented performances at least comparable with those of reference cells.

**Keywords:** *Organic solar cells, P3HT:PCBM films, CoFe2O4 nanoparticles, power conversion efficiency, stability and lifetime.*

## 1. Introduction

Recent advances towards improvement of the power conversion efficiency (PCE) of organic solar cells (OSC) have shown that the photovoltaic parameters depend mainly on the morphology of the active layer [1-3], the interfacial layers (electron and hole transporter layer) [4-7] and the architecture of devices [8,9].

The active layer is the most important component of an OSC. In the state of the art, it is composed of two different organic materials (a donor and an acceptor) with offset energy levels form nanometric domains in the bulk- heterojunction (BHJ) [5-7]. Experimental realization of this is a challenging task, and the behavior of the organic semiconductors can be hardly predicted in terms of forming interpenetrating phase-separation in BHJ solar cells. While most of the recent records of PCE are directly associated with BHJ morphology engineering [10,11], OSC performance can also be improved by extending excitons effective lifetime [12], thus attaining more efficient photogenerated charge carriers' collection [13,14]. This can be achieved by doping of the photoactive layer with oxide magnetic NPs.

Considerable improvement on power conversion efficiency of OSC has been achieved[8,9], and the organic photovoltaic technology is already commercially available. Moreover, studies of long-term stability of OSC has received considerable attention among several research groups and great efforts have been undertaken in order to find ways to extend their stability and lifetime making this technology increasingly attractive[15-18]. The major reasons and mechanisms for degradation of OSC device performance and parameters are widely documented in the literature. Organic solar cells degrade due to a number of factors, such as exposure to high temperatures and ultraviolet radiation[19-21], water or oxygen intake[22,23], as well as combinations of these factors[24,25]. Thus, in order to obtain a good insight of device stability and lifetime, it's essential to study the complete working device under various stresses and observe how the different photovoltaic parameters evolve with time.

In general, spinel ferrites are of a great interest in fundamental science, especially addressing the fundamental relationship between magnetic properties and their crystal chemistry and structure[26,27]. Notably, $CoFe_2O_4$ NPs possesses chemical, mechanical, magnetic and optical properties which make

*e-mail: mauriciosousa@alu.ufc.br.

them a promising candidate for technological applications[28]. Among the possible applications of $CoFe_2O_4$ NPs are their potential use as ferrofluids[27], biological treatment agents[29] and as a constituent part of photovoltaic solar cells[14,30].

Several research groups have reported that PCE and stability improvement has been achieved by introducing small amounts of magnetic NPs (such as spinel ferrites) in cells active layers[5,12-14,31,32]. The possible explanation to the observed improvement points in two directions: one proposition suggests that the dipole interactions from magnetic NPs induce a coercive electric field, which can contribute to the improvement of the photovoltaic parameters[13,32,33]; another proposition argues that the presence of magnetic moments within the active layer increases the number of excitons that are dissociated into charge carriers. This would be due to spin-orbit coupling which improves the efficiency of intersystem crossing[12].

The authors present a systematic study on the influence of $CoFe_2O_4$ NPs on the performance and stability of large area, flexible organic solar cells fabricated by a semi-industrial blade coating process using non-halogenated solvents. $CoFe_2O_4$ NPs were produced by the proteic sol-gel method and their structural and magnetic properties were investigated prior to cells construction. For this purpose, we use a system composed by poly(3-hexylthiophene-2,5-diyl) (P3HT) and [6,6]-phenyl-C61-butyric acid methyl ester (PCBM) blended with $CoFe_2O_4$ NPs substituting the P3HT in a ratio of 1:0.99 (in wt%). The tests of stability and lifetime were evaluated following the International Summit on OPV Stability (ISOS) protocols. The stability and lifetime tests indoor and outdoor were performed following the ISOS-L-1, ISOS-D-3 and ISOS-O-1 protocols during 1200 h for both sets of devices produced.

## 2. Experimental Procedure

### *2.1. Synthesis of $CoFe_2O_4$ nanoparticles*

$CoFe_2O_4$ NPs were produced by a proteic sol-gel method[34] following an experimental procedure described elsewhere[35,36]. Commercial $Fe(NO_3)_3\ 9H_2O$ (Sigma-Aldrich, 98%, 404 g/mol ) and $Co(NO_3)_2\ 6H_2O$ (Sigma-Aldrich, 98%, 291.03 g/mol) powders were used as metal precursors and comercial gelatin from bovine skin (Type B, Sigma-Aldrich) was used as organic precursor. Firstly, 2 g of gelatin was dispersed in distilled water under continuous stirring at room temperature (RT) until a uniform gel was obtained. Posteriorly, 2.648 g $Co(NO_3)_2\ 6H_2O$ and 7.352 g of $Fe(NO_3)_3\ 9H_2O$ were dissolved in distilled water to make a solution of $Co^{2+}$:$Fe^{3+}$ at a cobalt-to-iron molar ratio of 1:2. The solution containing metal ions was added to the gel and maintained under continuous stirring at RT for 2 h. This step aims to disperse the metal ions along the gelatin polymer chains in a process known as complexation and prevent that ions decant at the bottom of the container. The substance formed was dried at 150 ºC for 12 h to remove water excess resulting in a solid mass known as the precursor powder. The $Co^{2+}/Fe^{3+}$ precursor powder was calcined at 400 ºC for 4 h under air atmospheric conditions with a heating rate of 5 ºC/min, resulting in approximately 2.5 g of $CoFe_2O_4$ NPs. For economy of notation, $CoFe_2O_4$ NPs will sometimes be referred to as CFO.

### *2.2. Solar cell fabrication*

Flexible, large-area, inverted organic photovoltaic devices were fabricated and tested. An electron transport layer (undisclosed material due to patent pending issues) of 8 nm, a P3HT (Sigma-Aldrich):PCBM (Sigma-Aldrich)-based active layer of 300 nm, and a poly(3,4-ethylenedioxythiophene)-poly(styrenesulfonate) (PEDOT:PSS) (Sigma-Aldrich, low-conductivity grade) hole transport layer of 200 nm were deposited in sequence on a flexible substrate (polyethylene coated with an ITO/Ag/ITO multilayer with a resistance of 10 Ω/sq, via a semi-industrial blade coating process. To close the devices a 200 nm-thick Ag back electrode was deposited by thermal evaporation with a rate of 1 Å/s. The devices were built with an area of 0.55 $cm^2$.

Reference (ref-OSC) and CFO-bearing (CFO-OSC) devices were built for this study. Active layer blends of ref-OSC cells were made out of a 1:0.8 molar mixture of P3HT:PCBM dispersed in a mixture of o-xylene based nonhalogenated solvents. The CFO-OSC blends were comprised of a 0.99:0.01:0.8 mixture (in weight) of P3HT:CFO:PCBM. The NPs were suspended in o-xylene:tetralin (1 mg/mL) and mixed to the P3HT:PCBM blend to achieve the desired concentration.

Prior to testing, all samples were encapsulated with a barrier foil with a water vapor transmission rates (WVTR) of $10^{-3}$ g/$m^2$/day with an integrated ultraviolet (UV) cut-off at 385 nm, laminated with a UV curable adhesive. Sets with 10 ref-OSC and 10 CFO-OSC devices were prepared for the tests of efficiency and stability.

### *2.3. Characterization*

X-ray diffraction (XRD) of the nanostructured powders was carried out using a X-Pert PRO MPD Panalytical diffractometer operating with a Kα-Co source (λ = 1.788 Å). The pattern was Rietveld refined[37,38] using the GSAS program[39]. The magnetic measurement was performed using a Microsense EV9 model vibrating sample magnetometer. Mössbauer spectroscopy was carried out in transmission mode using a $^{57}$Co(Rh) radioactive source mounted on a velocity driver operating in sinusoidal mode. The spectrum was evaluated by least square fitting using the software package Normos. All measurements were carried out at room temperature. Transmission Electron Microscopy (TEM) was performed using a JEM 1011 - JEOL microscope.

Ultraviolet-visible (UV-Vis) spectroscopy of pure and doped P3HT:PCBM films were carried out using a UV 2600 Shimadzu spectrophotometer coupled to an integrating sphere ISR 2600

Plus. Atomic force microscopy (AFM) and conductive atomic force microscopy (C-AFM) measurements were performed using an Asylum Research scanning probe microscope. Images were collected in tapping mode using a Nanoworld (model Arrow CONTPt) Pt-coated Si probe with a spring constant of 0.2 N/m. All measurements were carried out at room temperature.

Solar simulations of photovoltaic devices were performed on a Wacon WXS-156S-10 model equipped with an AM 1.5 filter (100 mW/cm$^2$, AM 1.5 G). A calibrated Si/BK7 photodiode from PV measurements was also applied for calibration before each measurement.

## 3. Results and Discussion

### *3.1. $CoFe_2O_4$ nanoparticles*

Figure 1a shows the XRD pattern of a CFO sample. The XRD pattern was fitted using the Rietveld method and the best fit is showed as a solid red line. The Williamson-Hall curve[40] is shown in the inset of Fig. 1a. The diffractogram shows peaks that match the Inorganic Crystal Structure Database (ICSD) entry 84611 of the cubic crystal structure (Fd3m) of $CoFe_2O_4$ (bars in the Fig. 1a). No other crystalline phase was found. The lattice parameters were found to be a = b = c = 8.378 Å and crystallite average size to be $D_S$ = 6.0 nm as calculated by the Scherrer formula and $D_{WH}$ = 9.0 nm when corrected by the Williamson-Hall method after compensating for a residual microstrain ε of 0.009 %.

CFO NPs exhibited a typical ferromagnetic behavior at RT as can be seen from the hysteresis loop shown in Fig. 1b. The magnetic interactions in NPs are unstable and disordered, thus the magnetic moment cannot be easily kept to be consistent with the external field. Furthermore, the surface of the NPs seems to be composed of some distorted or slanted spins that repel the core spins to align the field direction. The values obtained here are in agreement with others reported in the literature[41-43]. The inset of Fig. 1b shows the room temperature Mössbauer spectrum of a CFO sample. The spectrum showed a superposition of a sextet and a doublet. In general, $CoFe_2O_4$ with spinel structure exhibits ferrimagnetic properties characterized by two sextets in the Mössbauer spectrum[42]. The central doublet present in the spectrum is assigned to a fraction of the compound that possesses a superparamagnetic character. Therefore, the CFO sample shows ferrimagnetic and superparamagnetic interactions, simultaneously.

Prior to the TEM analysis, the NPs were dispersed in ethanol at a ratio of 1mg / 1ml and sonicated for 1h to avoid aggregates. Subsequently, a drop of the mixture was deposited on a nanometer grid. Figure 2 shows TEM images (two different magnifications) of a CFO sample. It can be seen that CFO NPs have an approximate spherical morphology with an average diameter between 4 and 10 nm (see Fig. 2c), in good agreement with the sizes obtained from the XRD data.

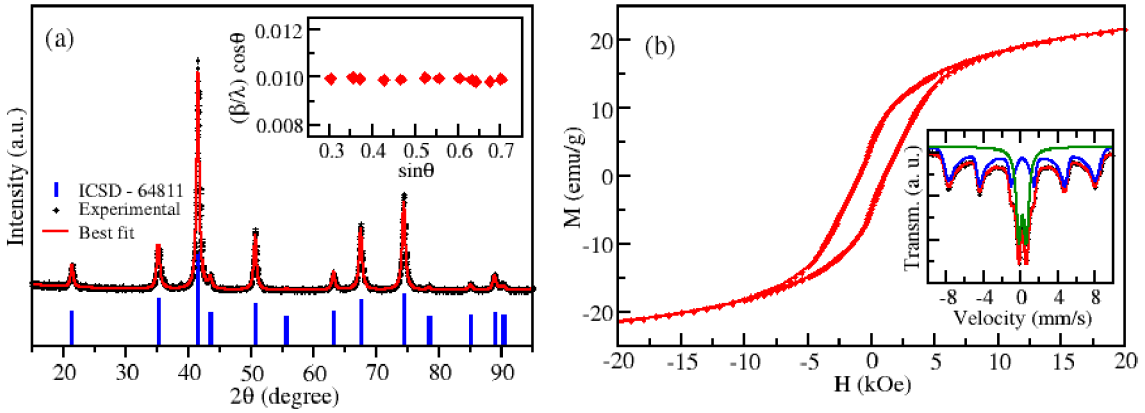


**Figure 1. (a)** X-ray diffraction pattern of a CFO sample. Dots and solid line are the experimental data and best fit respectively. Bars represent the ICSD-64811 standard pattern. *Inset*: Williamson-Hall curve. **(b)** Room temperature hysteresis loop of a CFO sample. *Inset*: Mössbauer spectrum of a CFO sample. Dots and solid line are the experimental data and best fit respectively.

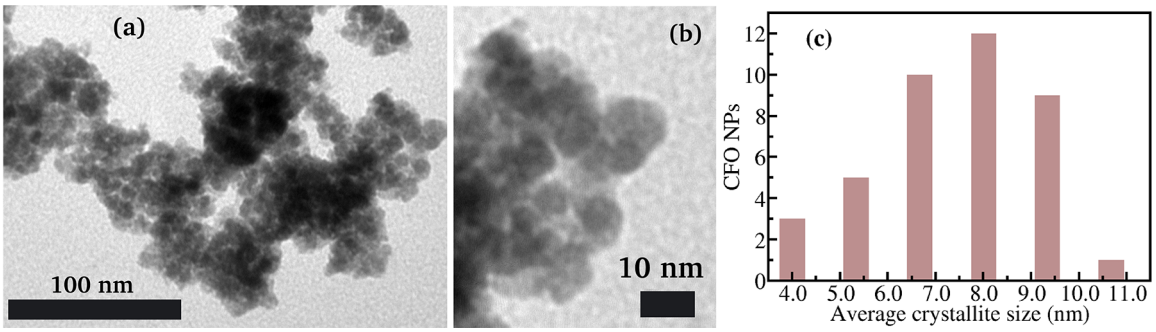


**Figure 2.** TEM imagens of CFO NPs (two magnifications) and average crystallite size distribution histograms.

### *3.2. Active layer characterization*

Figure 3 shows UV-vis absorption spectra of P3HT:PCBM (ref-OSC) and P3HT:CFO:PCBM (CFO-OSC) films. The main absorption band is found around the wavelength 520 nm which is atributed to $\pi$ - $\pi^*$ transition of P3HT conjugated backbone, whereas the two shoulders around 550 and 600 nm are ascribed to the extended conjugated P3HT and the inter-chain stacking of P3HT, respectively; these two bands indicate a well-order structure. The discrete absorption peak around 332 nm is assigned to the PCBM[7,44].

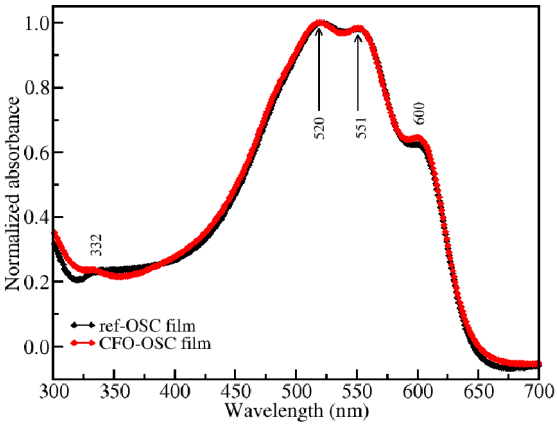


**Figure 3.** UV-Vis absorbance spectra of ref-OSC and CFO-OSC films.

Comparing the absorption spectra of ref-OSC and CFO-OSC samples, one can observed that they do not present significant variations. This suggests that addition of NPs did not contribute significantly to the increase or decrease of the radiation absorption by P3TH in active layer.

Figure 4 shows AFM images of ref-OSC and CFO-OSC films. In the CFO-OSC films the NPs used in this application have average sizes of the order of 4-10 nm, in addition they represent a small fraction of the active layer mass (1 wt% to P3HT). It can be observed on the AFM surface topography images - ref-OSC film: Figs. 4a and b; CFO-OSC film: Figs. 4e and d – that the addition of NPs a in this ratio did not affect the morphology of the film, suggesting that the NPs are homogeneously distributed within the film without the formation of agglomerates.

Current AFM images - ref-OSC film: Fig. 4c; CFO-OSC film: Fig. 4f - was used to examine conductivity variations in the P3HT:PCBM pristine and doped blends. A high work function Pt-coated Si probe was used in all measurements. The high electron injection barrier between the Pt-coated Si tip and the P3HT:PCBM blend blocks electron injection which allows hole transport only within P3HT [45,46]. Therefore, bright and dark regions are attributed to P3HT-rich and PCBM-rich domains, respectively. In both cases, it was observed a homogeneous distribution in the current images, suggesting that the NPs are not contributing significantly to eventual variations of currents through the active layer.

### *3.3. Solar cells characterization*

Figure 5 shows a typical current density versus voltage curve (J×V) measured under simulated AM 1.5 solar illumination at 100 mW/cm$^2$. A set of 10 devices of each type was analyzed and the average values of the photovoltaic parameters are summarized in Table 1. Small standard deviations are a result of highly reproducible values, which is an indicator of the quality of the manufacturing process.

According to the data shown in Table 1 the devices reinforced with CFO showed a 10 % increase in PCE when compared to the reference devices. In general, PCE is determined by short-circuit current density ($J_{sc}$), open circuit voltage ($V_{oc}$) and fill factor (FF). In BHJ OSC, the $J_{sc}$ value of an OSC depends strongly on the gap energy[12,14], $V_{oc}$ depends on the energy difference between the lowest unoccupied molecular orbital (LUMO) of the acceptor and the highest occupied molecular orbital (HOMO) of the donor[7] and FF is a critical parameter that can reflect dynamic transport of the photocurrent in OSC[10].

Once $V_{oc}$ and FF remain virtually unchanged, this increase on PCE is due to a larger $J_{sc}$. From the UV-vis absorption spectra of ref-OSC and CFO-OSC films, it can be seen that doping of the P3HT:PCBM active layer did not significantly affect the absorption spectra. Therefore, this suggests that the increase in $J_{sc}$ is not related to the absorption of incident light. The incorporation of NPs to the active layer likely creates mechanisms that provide an improvement in the collection of photogenerated charge carriers.

Two possible explanations have been proposed in the literature. One of the propositions is that the presence of a coercive electric field (CEF) produced by the dipole interactions between CFO nanoparticles could assist the built-in electric field on the collection of charge carriers by the electrodes[13,32,33]. The other one argues that the presence of magnetic moments within the active layer increases the efficiency of intersystem crossing that extends exciton lifetime and diffusion length[12].

It is known that in organic materials such as P3HT the primary photo-generated charge carriers are Coulomb-bound electron-hole pairs, so-called excitons, which lie in both singlet states and triplet states with different lifetimes[47,48]. In photovoltaic devices only the dissociated excitons could contribute to the photocurrent. In P3HT the singlet lifetime is approximately 300 ps and the resulting singlet exciton diffusion length is reported in the range of 3-6 nm[47]. In contrast, the P3HT triplet lifetime is in the order of 10 ms implying a triplet exciton diffusion length of the order of 100 nm[48], which aids their diffusion process toward donor-acceptor junctions and thus enhances the photovoltaic process in OSCs. The migration of excitonic states from the excited singlet to the triplet can occur in the presence of strong spin-orbit coupling[12]. This transition is known as intersystem crossing. Longer living excitons reach a donor-acceptor interface in larger numbers which increases their dissociation rate into free charge carriers. This issue remains open to further investigation.

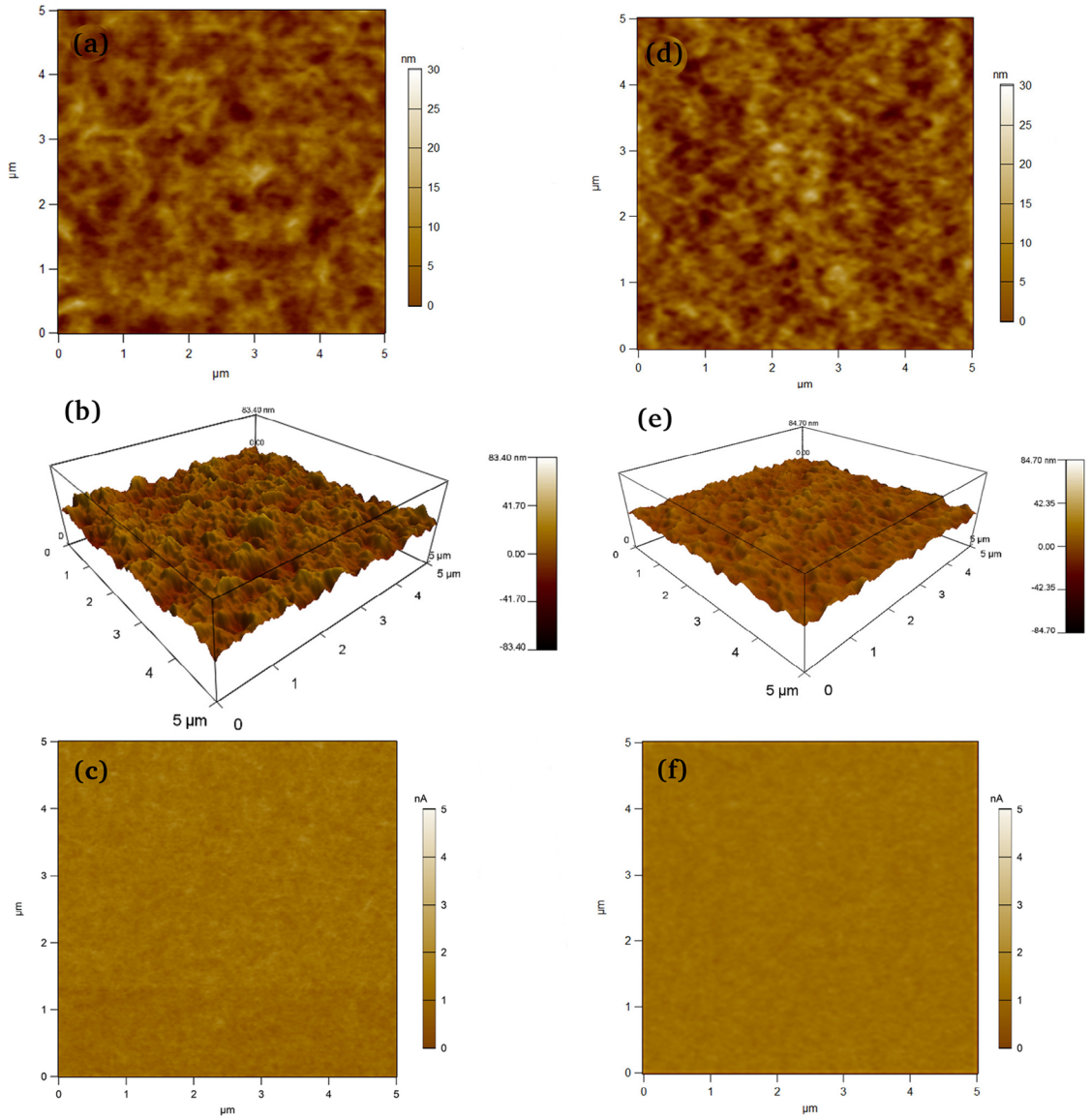


**Figure 4. (a)** AFM morphology image, **(b)** height images of the surface morphology and **(c)** C-AFM current images of a ref-OSC film; **(d)** AFM morphology image, **(e)** height images of the surface morphology and **(f)** C-AFM current images of a CFO-OSC film.

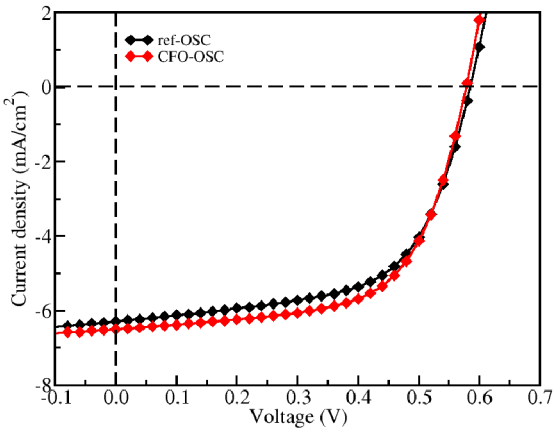


**Figure 5.** J×V curves of the best ref-OSC and CFO-OSC cells. Under illumination AM 1.5 with the light intensity of 100 mW/cm$^2$.

**Table 1.** Photovoltaic parameters of ref-OSC and CFO-OSC devices under simulated AM 1.5 solar illumination at 100 mW/cm$^2$. $J_{sc}$, $V_{oc}$, FF, PCE are: short-circuit current density, open circuit voltage, fill factor and power conversion efficiency, respectively.

| Device | $J_{sc}$ (mA/cm$^2$) | $V_{oc}$ (Volt) | FF (%) | PCE (%) |
|---|---|---|---|---|
| ref-OSC | 5.9±0.2 | 0.58±0.01 | 61.0±1.0 | 2.00±0.1 |
| CFO-OSC | 6.3±0.3 | 0.57±0.01 | 62.0±0.4 | 2.20±0.1 |

## *3.4. Lifetime and stability studies*

An important part of understanding degradation mechanisms is the proper evaluation of solar cells performance submitted to different degradation conditions as a function of time. There are several stability test categories for OSC devices

such as tests under dark, simulated light and humidity and at outdoor conditions. Each degradation test is divided into three categories: basic, intermediate, and advanced levels[16,49]. The main parameters of the experiments are temperature, light, humidity, and environment. There are several factors and mechanisms for degradation of OSC devices such as light exposure[15,19,20], high temperatures[21,49], low resistance to water and oxygen[22,23], as well as combinations of these factors[24,25].

In this work, stability and lifetime tests of ref-OSC and CFO-OSC devices were performed according to the International Summit on OPV Stability (ISOS) protocols. The stability and lifetime tests were performed for 1200 h following the ISOS-D-3, ISOS-O-1, and ISOS-L-1 standards. These experiments are outlined in Table 2. The samples submitted to the ISOS-D-3 and ISOS-O-1 tests were periodically removed from the degradation platform and measured indoors under a calibrated solar simulator with AM1.5G spectrum and 100 mW/cm$^2$of illumination. In order to obtain a considerable amount of data, the stability and lifetime tests were performed for a set of ten devices for each experiment and the average values are shown in the plots.

### *3.4.1. ISOS-D-3 test*

The measurement of lifetime and stability of OSC under high temperature and humidity is an important requirement of practical deployment of these devices. ISOS-D-3 tests were performed according to the conditions described on Table 2. The time evolution of photovoltaic parameters and resistances normalized to their pre-test values is shown in Fig. 6. The normalized PCE values of ref-OSC and CFO-OSC submitted to ISOS-D-3, ISOS-O-1 and ISOS-L-1 tests are summarized in Table 3.

Fig. 6a shows that T 80 for PCE was reached just after ~380 h for both sets of devices. This fast degradation can be explained by the very rough conditions of the test. After 740 h of testing, the CFO-OSC devices started to demonstrate slightly better ability to keep PCE when compared with the ref-OSC devices, maintaining this behavior until the end of the experiment. The PCE of ref-OSC lowered to about 50 % of the initial value whereas for CFO-OSC the PCE stayed at about 60 % at the end of the test. These results can be taken as indication that the use of CFO has the potential to improve cells' lifetime and stability in very rough conditions, which can be translated into longer lifetimes in real operational situations.

Only a small decrease in $J_{sc}$ was observed during the test, with a slightly better performance of CFO-OSC cells towards the end of the test (Fig. 6b). Values of $V_{oc}$ for both set of devices remained virtually unchanged during the test (Fig. 6c), which indicates unchanged polymer and fullerene energy levels. Therefore, the decrease in PCE observed was due mainly to the FF reduction seen in Fig. 6d. In fact, both PCE and FF curves follow the same trend. Fig.s 6e and 6f show a four-fold increase in $R_s$ and a 40 % decrease in $R_{sh}$ which is attributed to a large amount of water uptake in the

**Table 2.** ISOS protocols used for lifetime and stability testing of OSC.

| Testing ID | Testing conditions | | | |
|---|---|---|---|---|
| | Light source | Temperature | Humidity | Environment |
| ISOS-D-3 | None | 85 ◦ C | 85% | Climate chamber |
| ISOS-O-1 | Sunlight | Ambient | Ambient | Outdoor |
| ISOS-L-1 | Solar Simulator | Ambient | Ambient | Solar Simulator |

**Table 3.** Normalized PCE values of ref-OSC and CFO-OSC submitted to ISOS-D-3, ISOS-O-1 and ISOS-L-1 tests.

| Testing ID | ISOS-D-3 test | | ISOS-L-1 test | | ISOS-L-1 test | |
|---|---|---|---|---|---|---|
| | Normalized PCE | | | | | |
| Exposute time (h) | ref-OSC | CFO-OSC | ref-OSC | CFO-OSC | ref-OSC | CFO-OSC |
| 0.0 | 1.000 | 1.000 | 1.000 | 1.000 | 1.000 | 1.000 |
| 49.0 | 0.956 | 0.956 | 0.989 | 0.982 | 0.864 | 0.934 |
| 92.2 | 0.943 | 0.897 | 0.971 | 0.980 | 0.906 | 0.904 |
| 190.0 | 0.889 | 0.926 | 0.976 | 0.980 | 0.885 | 0.884 |
| 233.0 | 0.891 | 0.937 | 0.979 | 0.980 | 0.880 | 0.897 |
| 378.0 | 0.788 | 0.813 | 0.959 | 0.967 | 0.863 | 0.877 |
| 498.0 | 0.765 | 0.729 | 0.940 | 0.951 | 0.810 | 0.812 |
| 863.0 | 0.680 | 0.663 | 0.943 | 0.963 | 0.835 | 0.856 |
| 1097.7 | 0.622 | 0.651 | 0.919 | 0.921 | 0.811 | 0.842 |
| 1194.0 | 0.532 | 0.592 | 0.925 | 0.920 | 0.809 | 0.835 |

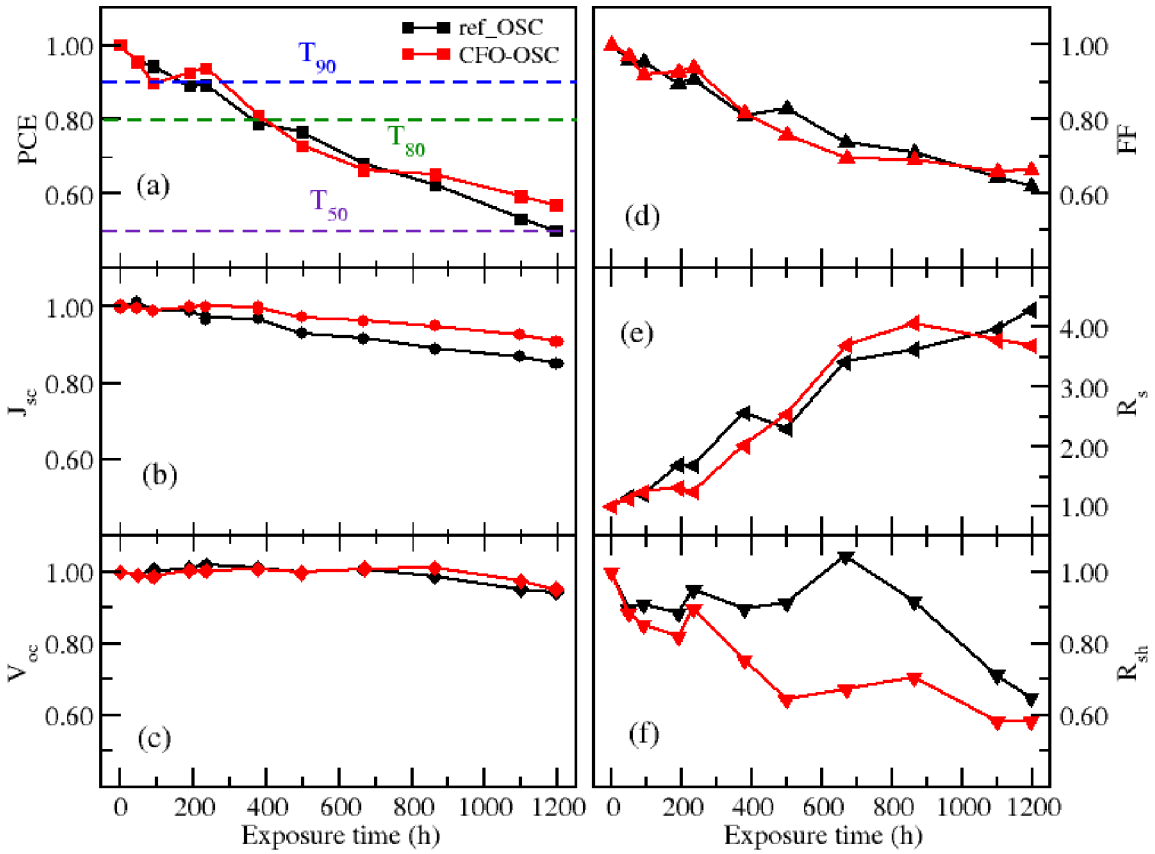


**Figure 6.** ISOS-D-3 test: time evolution of (a) PCE, (b) $J_{sc}$, (c) $V_{oc}$, (d) FF, (e) $R_s$ and (f) $R_{sh}$ of ref-OSC (black) and CFO-OSC (red) devices. All quantities are normalized to their initial pre-test values.

testing chamber. As is well known, FF values are strongly affected by series and shunt resistances.

*3.4.2. ISOS-O-1 test*

The devices were tested in real outdoor conditions following the ISOS-O-1 protocol with details described in Table 2. The devices were tested for 1200 h at the CSEM Brazil facilities in Belo Horizonte, Brazil, located at 19 ◦ 55' 15" S latitude and 43 ◦ 56' 16" W longitude. This experiment was carried out between September and October of 2018. The maximum ambient testing temperature was 28 ºC. The time evolution of photovoltaic parameters and resistances normalized to their pre-test values is shown in Fig. 6.

Fig. 7a shows a decrease in PCE to about 80% of the pre-test values, with similar behavior for the ref-OSC and CFO-OSC devices. The initial strong drop in $J_{sc}$ values (Fig. 7b) is referred to as burn-in[21,22], which is a signature of light induced degradation[24]. This burn-in has been demonstrated to be related to the photoinduced dimerization of fullerenes within the active layer [50,51]. The larger drop for CFO-OSC is attributed to the higher absolute $J_{sc}$ initial value. Samples with higher values of $J_{sc}$ are more sensitive to photoinduced dimerization.

Values of $V_{oc}$ and FF are presented in Figs. 6c and 6d and showed very little variation during the test. It indicates the absence of any major degradation mechanism other than photodimerization. The fill factors presented a slightly increase over time with consistent larger values for the CFO-OSC devices which can be related to a more efficient collection of charge carriers. Series and shunt resistances did not present considerable variation over the duration of test (Figs. 6e and 6f).

The similar degradation behavior of both sets of devices does not allow for an assessment of the role of NPs in the cells' stability in real outdoor conditions. It is possible that the test performed for this work did not last long enough to notice any benefit from the presence of NPs in the active layer. In order to evaluate the effect in longer light exposure times, accelerated tests according to the ISOS-L-1 protocol were carried out and are the results are presented below.

*3.4.3. ISOS-L-1 test*

ISOS-L-1 tests were performed according to the conditions described on Table 2. The time evolution of photovoltaic parameters and resistances normalized to their pre-test values is shown in Fig. 8.

Fig. 8a shows a quick decrease in PCE for both devices during the first 50 hours of testing. This reduction is more evident in the reference devices. The initial strong drop is

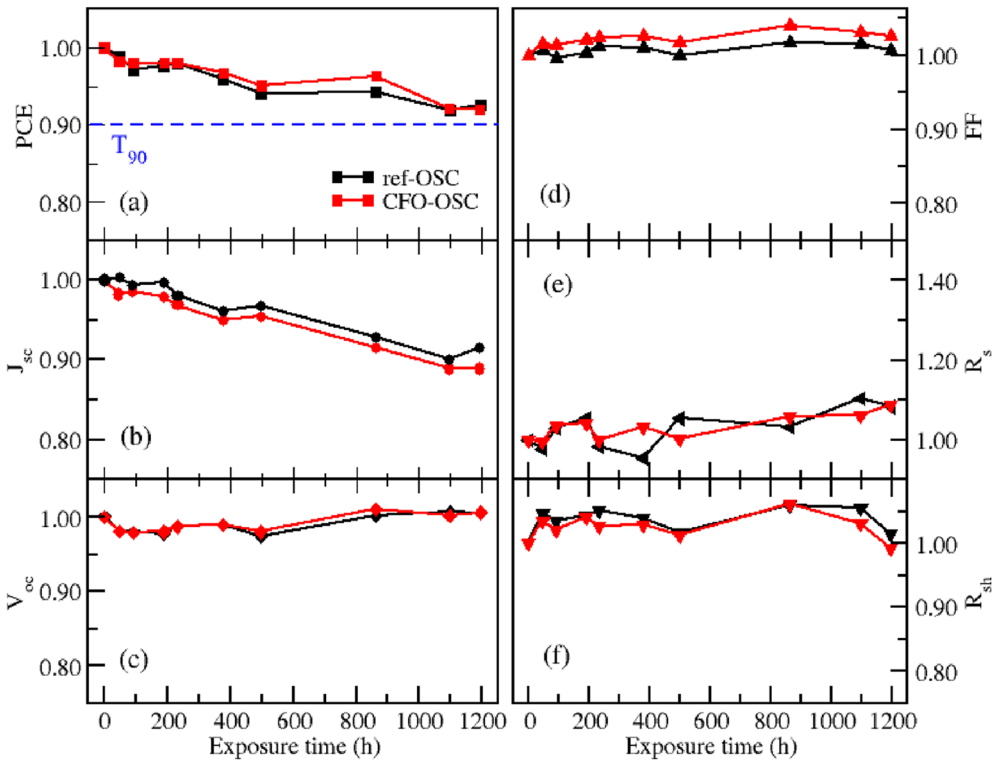


**Figure 7.** ISOS-O-1 test: time evolution of (a) PCE, (b) $J_{sc}$, (c) $V_{oc}$, (d) FF, (e) $R_s$ and(f) $R_{sh}$ of ref-OSC (black) and CFO-OSC (red) devices. All quantities normalized to their initial values.

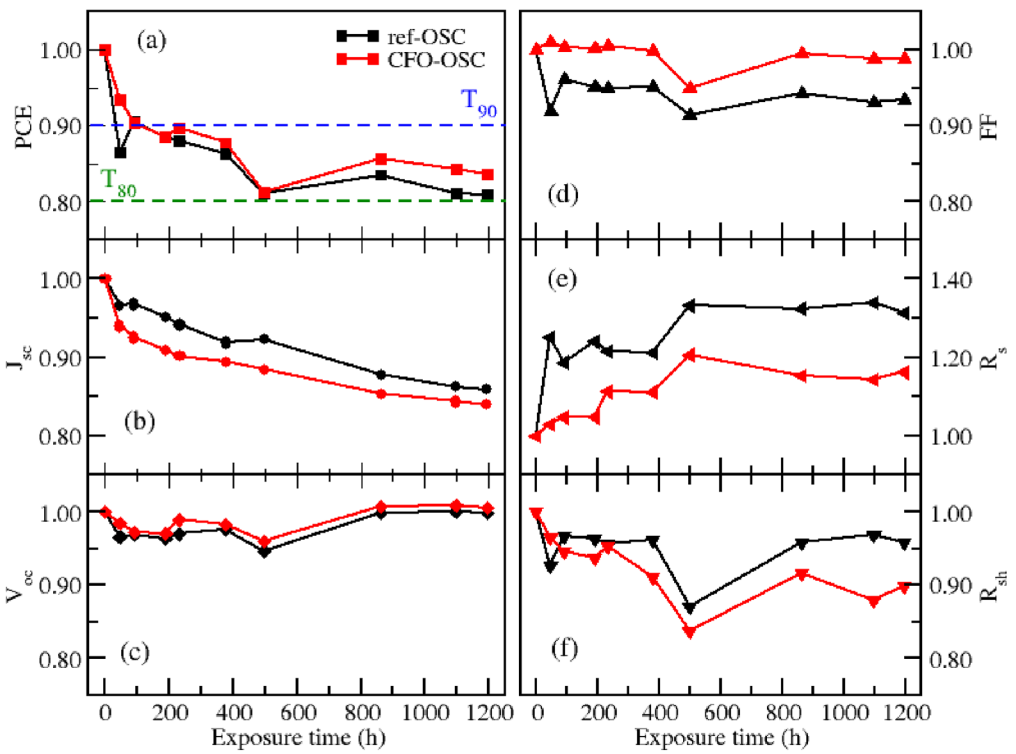


**Figure 8.** ISOS-L-1 test: time evolution of (a) PCE, (b) $J_{sc}$, (c) $V_{oc}$, (d) FF, (e) $R_s$ and (f) $R_{sh}$ of ref-OSC (black) and CFO-OSC (red) devices. All quantities normalized to their to initial values.

attributed to the photoinduced dimerization of fullerenes within the active layer. At the end of the test the PCE values decreased less than 20 % of the initial values, which is a very respectful result for P3HT:PCBM-based cells aged under open circuit condition. Fig. 8b shows a slightly larger drop in $J_{sc}$ for the CFO-OSC samples, which can be explained by their higher initial value. Despite the slightly larger drop in $J_{sc}$, the CFO-OSC devices were more likely to retain their PCE than the ref-OSC devices.

Because $V_{oc}$ remains almost constant during the whole test, this ability to PCE even with a larger sensitivity to photoinduced dimerization can be explained by superior performance regarding to FF as shown in Fig. 8d. The CFO-OSC devices were able to keep almost the same FF during the entire duration of the test, while ref-OSC samples presented a drop in FF of over 5%. As mentioned before, FF values are strongly affected by the series and shunt resistances, therefore the lower FF of ref-OSC devices can explained by a more severe degradation of the series resistance over time as can be seen in Fig. 8e. This suggests that the presence of CFO contributes effectively to the improvement of the diffusion and collection of charge carriers, as bulk resistance is more likely to be affected by increments in series resistance.

## 4. Conclusion

CFO with average crystal size around 9 nm were successfully synthesized using the proteic sol-gel method and applied to bulk-heterojunction organic solar cells. Pure and NP-doped blends of P3HT:PCBM were dispersed in a mixture of o-xylene based non-halogenated solvents and deposited via a semi-industrial blade coating process on flexible substrates to fabricate large area (0.55 $cm^2$), flexible organic solar cells with inverted configuration. Optimization of cells active layer through the incorporation of CFO resulted in an increased $J_{sc}$ and, as a result, a conversion efficiency enhancement of about 10% with respect to the reference devices. Reference and doped devices were subjected to stability and lifetime tests according to the ISOS-D-3, ISOS-O-1 and ISOS-L-1 protocols. Results showed that doped cells presented performances at least comparable with those of reference cells for the duration of the tests. Doped cell performed better during the ISOS-L-1 test suggesting that presence of CFO contributes effectively to the improvement of the diffusion and collection of charge carriers.

## 5. Acknowledgements

The authors are grateful to the Brazilian research agencies Fundação Cearense de Apoio ao Desenvolvimento Científico Tecnológico (FUNCAP), Coordenação de Aperfeiçoamento de Pessoal de Nível Superior (CAPES) and Conselho Nacional de Desenvolvimento Científico e Tecnológico (CNPq) for financial support. The authors would also like to thank the Central Analítica-UFC/CT-INFRA/MCTI-SISNANO/Pró-Equipamentos CAPES for the support.

## 6. References

1. Ameen MY, Shamjid P, Abhijith T, Reddy VS. Solution processed transition metal oxide anode buffer layers for efficiency and stability enhancement of polymer solar cells. *Optical Materials*. 2018;75:491-500.

2. Scharber MC, Sariciftci NS. Efficiency of bulk-heterojunction organic solar cells. *Progress in Polymer Science*. 2013;38(12):1929-1940.

3. Huang YC, Cha HC, Chen CY, Tsao CS. Morphological control and performance improvement of organic photovoltaic layer of roll-to-roll coated polymer solar cells. *Solar Energy Materials and Solar Cells*. 2016;150:10-18.

4. Zafar M, Yun JY, Kim DH. Improved inverted-organic-solar-cell performance via sulfur doping of ZnO films as electron buffer layer. *Materials Science in Semiconductor Processing*. 2019;96:66-72.

5. Pereira MS, Lima FAS, Ribeiro TS, da Silva MR, Almeida RQ, Barros EB, et al. Application of Fe-doped $SnO_2$ nanoparticles in organic solar cells with enhanced stability. *Optical Materials*. 2017;64:548-556.

6. Tran VH, Khan R, Lee IH, Lee SH. Low-temperature solution-processed ionic liquid modified $SnO_2$ as an excellent electron transport layer for inverted organic solar cells. *Solar Energy Materials and Solar Cells*. 2018;179:260-269.

7. Kadem BY, Kadhim RG, Banimuslem H. Efficient P3HT:SWCNTs hybrids as hole transport layer in P3HT:PCBM organic solar cells. *Journal of Materials Science: Materials in Electronics*. 2018;29(11):9418-9426.

8. Zhao W, Li S, Yao H, Zhang S, Zhang Y, Yang B, et al. Molecular Optimization Enables over 13% Efficiency in Organic Solar Cells. *Journal of the American Chemical Society*. 2017;139(21):7148-7151.

9. Xiao Z, Jia X, Ding L. Ternary organic solar cells offer 14% power conversion efficiency. *Science Bulletin*. 2017;62(23):1562-1564.

10. Gasparini N, Salvador M, Heumueller T, Richter M, Classen A, Shrestha S, et al. Polymer:Nonfullerene Bulk Heterojunction Solar Cells with Exceptionally Low Recombination Rates. *Advanced Energy Materials*. 2017;7(22):1701561.

11. Veerender P, Saxena V, Chauhan AK, Koiry SP, Jha P, Gusain A, et al. Probing the annealing induced molecular ordering in bulk heterojunction polymer solar cells using in-situ Raman spectroscopy. *Solar Energy Materials and Solar Cells*. 2014;120(Pt B):526-535.

12. González DM, Körstgens V, Yao Y, Song L, Santoro G, Roth SV, et al. Improved Power Conversion Efficiency of P3HT:PCBM Organic Solar Cells by Strong Spin-Orbit Coupling-Induced Delayed Fluorescence. *Advanced Energy Materials*. 2015;5(8):1401770.

13. Wang K, Yi C, Liu C, Hu X, Chuang S, Gong X. Effects of Magnetic Nanoparticles and External Magnetostatic Field on the Bulk Heterojunction Polymer Solar Cells. *Scientific Reports*. 2015;5:9265.

14. Kovalenko A, Yadav RS, Pospisil J, Zmeskal O, Karashanova D, Heinrichová P, et al. Towards improved efficiency of bulk-heterojunction solar cells using various spinel ferrite magnetic nanoparticles. *Organic Electronics*. 2016;39:118-126.

15. Zhang Y, Yi H, Iraqi A, Kingsley J, Buckley A, Wang T, et al. Comparative indoor and outdoor stability measurements of polymer based solar cells. *Scientific Reports*. 2017;7:1305.

16. Benatto GAR, Roth B, Corazza M, Søndergaard RR, Gevor-Gyan SA, Jørgensen M, et al. Roll-to-roll printed silver nanowires for increased stability of flexible ITO-free organic solar cell modules. *Nanoscale*. 2016;8(1):318-326.

17. Wu Z, Yu Z, Yu H, Huang X, Chen M. Effect of trifluoroacetic acid treatment of PEDOT:PSS layers on the performance and stability of organic solar cells. *Journal of Materials Science: Materials in Electronics*. 2018;29(8):6607-6618.

18. Kankanan M, Kosarian A, Farshidi E. Stability enhancement of ITO-free non-inverted PTB7:$PC_{71}$BM solar cell using two-step post-treated PEDOT:PSS. *Journal of Materials Science: Materials in Electronics*. 2018;29(14):12387-12398.

19. Lima FAS, Beliatis MJ, Roth B, Andersen TR, Bortoti A, Reyna Y, et al. Flexible ITO-free organic solar cells applying aqueous solution-processed $V_2O_5$ hole transport layer: An outdoor stability study. *APL Materials*. 2016;4(2):026104.

20. Chander N, Sing S, Iyer SSK. Stability and reliability of P3HT:PC61BM inverted organic solar cells. *Solar Energy Materials and Solar Cells*. 2017;161:407-415.

21. Tamai Y, Ohkita H, Namatame M, Marumoto K, Shimomura S, Yamanari T, et al. Light-Induced Degradation Mechanism in Poly(3-hexylthiophene)/Fullerene Blend Solar Cells. *Advanced Energy Materials*. 2016;6(11):1600171.

22. Rivaton A, Chambon S, Manceau M, Gardette JL, Lemaître N, Guillerez S. Light-induced degradation of the active layer of polymer-based solar cell. *Polymer Degradation and Stability*. 2010;95(3):278-284.

23. Kawano K, Pacios R, Poplavskyy D, Nelson J, Bradley DDC, Durrant JR. Degradation of organic solar cells due to air exposure. *Solar Energy Materials and Solar Cells*. 2006;90(20):3520-3530.

24. Madogni VI, Kounouhéwa B, Akpo A, Agbomahéna M, Hounkpatin SA, Awanou CN. Comparison of degradation mechanisms in organic photovoltaic devices upon exposure to a temperate and a subequatorial climate. *Chemical Physics Letters*. 2015;640:201-214.

25. Cheng P, Zhan X. Stability of organic solar cells: challenges and strategies. *Chemical Society Reviews*. 2016;45(9):2544-2582.

26. Hajalilou A, Mazlan SA, Abbasi M, Lavvafi H. Fabrication of spherical $CoFe_2O_4$ nanoparticles *via* sol-gel and hydrothermal methods and investigation of their magnetorheological characteristics. *RSC Advances*. 2016;6(92):89510-89522.

27. Kamali S, Pouryazdan M, Ghafari M, Itou M, Rahman M, Stroeve P, et al. Magnetization and stability study of a cobalt-ferrite-based ferrofluid. *Journal of Magnetism and Magnetic Materials*. 2016;404:143-147.

28. Royer F, Jamon D, Rousseau JJ, Zins D, Cabuil V, Neveu S, et al. Magneto-optical properties of $CoFe_2O_4$ ferrofluids. Influence of the nanoparticle size distribution. *Progress in Colloid and Polymer Science*. 2004;126:155-158.

29. Kanagesan S, Aziz SBA, Hashim M, Ismail I, Tamilselvan S, Alitheen NB, et al. Synthesis, Characterization and in Vitro Evaluation of Manganese Ferrite ($MnFe_2O_4$) Nanoparticles for Their Biocompatibility with Murine Breast Cancer Cells (4T1). *Molecules*. 2016;21(3):312.

30. Pang B, Lin S, Shi Y, Wang Y, Chen Y, Ma S, et al. Synthesis of $CoFe_2O_4$/graphene composite as a novel counter electrode for high performance dye-sensitized solar cells. *Electrochimica Acta*. 2019;297:70-76.

31. Wang K, Ren H, Yi C, Liu C, Wang H, Huang L, et al. Solution-Processed $Fe_3O_4$ Magnetic Nanoparticle Thin Film Aligned by an External Magnetostatic Field as a Hole Extraction Layer for Polymer Solar Cells. *ACS Applied Materials & Interfaces*. 2013;5(20):10325-10330.

32. Gong X, Jiang Y, Zhang C, Yang L, Li M, Ma H. Investigation of the magnetic nickel nanoparticles on performance improvement of P3HT:PCBM solar cell. *Applied Physics A*. 2016;122:287.

33. Zhang W, Xu Y, Wang H, Xu C, Yang S. $Fe_3O_4$ nanoparticles induced magnetic field effect on efficiency enhancement of P3HT:PCBM bulk heterojunction polymer solar cells. *Solar Energy Materials and Solar Cells*. 2011;95(10):2880-2885.

34. Meneses CT, Flores WH, Garcia F, Sasaki JM. A simple route to the synthesis of high-quality NiO nanoparticles. *Journal of Nanoparticle Research*. 2007;9(3):501-505.

35. Pereira MS, Lima FAS, Silva CB, Freire PTC, Vasconcelos IF. Structural, morphological and optical properties of $SnO_2$ nanoparticles obtained by a proteic sol-gel method and their application in dye-sensitized solar cells. *Journal of Sol-Gel Science and Technology*. 2017;84(1):206-213.

36. Pereira MS, Ribeiro TS, Lima FAS, Santos LPM, Silva CB, Freire PTC, et al. Synthesis and properties of $Sn_{1-x}Fe_xO_2$ nanoparticles obtained by a proteic sol-gel method. *Journal of Nanoparticle Research*. 2018;20:212.

37. Rietveld HM. Line profiles of neutron powder diffraction peaks for structure refinement. *Acta Crystallographica*. 1967;22(1):151-152.

38. Rietveld HM. A profile refinement method for nuclear and magnetic structures. *Journal of Applied Crystallography*. 1969;2:65-71.

39. Toby BH. EXPGUI, a graphical user interface for *GSAS*. *Journal of Applied Crystallography*. 2001;34(Pt 2):210-213.

40. Williamson GK, Hall WH. X-ray line broadening from filed aluminium and wolfram. *Acta Metallurgica*. 1953;1(1):22-31.

41. Nogueira NAS, Utuni VHS, Silva YC, Kiyohara PK, Vasconcelos IF, Miranda MAR, et al. X-ray diffraction and Mossbauer studies on superparamagnetic nickel ferrite ($NiFe_2O_4$) obtained by the proteic sol-gel method. *Materials Chemistry and Physics*. 2015;163:402-406.

42. Babić-Stojić B, Jokanović V, Milivojević D, Jagličić Z, Makovec D, Jović N, et al. Magnetic and Structural Studies of $CoFe_2O_4$ Nanoparticles Suspended in an Organic Liquid. *Journal of Nanomaterials*. 2013;2013:741036.

43. Mørup S, Hansen MF, Frandsen C. Magnetic interactions between nanoparticles. *Beilstein Journal of Nanotechnology*. 2010;1:182-190.

44. Sahare S, Veldurthi N, Datar S, Bhave T. Photon assisted conducting atomic force microscopy study of nanostructured additives in P3HT:PCBM. *RSC Advances*. 2015;5(124):102795-102802.

45. Dante M, Peet J, Nguyen TQ. Nanoscale Charge Transport and Internal Structure of Bulk Heterojunction Conjugated Polymer/Fullerene Solar Cells by Scanning Probe Microscopy. *The Journal of Physical Chemistry C*. 2008;112(18):7241-7249.

46. Chen FC, Ko CJ, Wu JL, Chen WC. Morphological study of P3HT:PCBM blend films prepared through solvent annealing for solar cell applications. *Solar Energy Materials and Solar Cells*. 2010;94(12):2426-2430.

47. Yao EP, Tsai YJ, Hsu WC. An investigation of organic photovoltaics improvement *via* extension of the exciton lifetime. *Physical Chemistry Chemical Physics*. 2015;17(8):5826-5831.

48. Xu B, Holdcroft S. Phosphorescence and delayed fluorescence of poly(3-hexylthiophene) films. *Thin Solid Films*. 1994;242(1-2):174-177.

49. Reese MO, Gevorgyan SA, Jørgensen M, Bundgaard E, Kurtz SR, Ginley DS, et al. Consensus stability testing protocols for organic photovoltaic materials and devices. *Solar Energy Materials and Solar Cells*. 2011;95(5):1253-1267.

50. Hermerschmidt F, Savva A, Georgiou E, Tuladhar SM, Durrant JR, McCulloch I, et al. Influence of the Hole Transporting Layer on the Thermal Stability of Inverted Organic Photovoltaics Using Accelerated-Heat Lifetime Protocols. *ACS Applied Materials & Interfaces*. 2017;9(16):14136-14144.

51. Heumueller T, Mateker WR, Distler A, Fritze UF, Cheacharoen R, Nguyen WH, et al. Morphological and electrical control of fullerene dimerization determines organic photovoltaic stability. *Energy & Environmental Science*. 2016;9(1):247-256.